Terahertz response of monolayer and few-layer WTe$_2$ at the nanoscale

Ran Jing[1], Yinming Shao[1], Zaiyao Fei[2], Chiu Fan Bowen Lo, Francesco L. Ruta[1], John Staunton[1], Alexander S. Mcleod[1], Zhiyuan Sun[1], Xinzhong Chen[3], Michael M. Fogler[4], Mengkun Liu[3,6], David H. Cobden[2], Xiaodong Xu[2,5] and D. N. Basov[1]

[1]Department of Physics, Columbia University, New York, NY, USA

[2]Department of Physics, University of Washington, Seattle, WA, USA

[3]Department of Physics and Astronomy, Stony Brook University, Stony Brook, NY, USA

[4]Department of Physics, University of California, San Diego, San Diego, CA, USA
[5]Department of Material Science and Engineering, University of Washington, Seattle, WA, USA

[6]National Synchrotron Light Source II, Brookhaven National Laboratory, Upton, NY, USA

Abstract: Tungsten ditelluride (WTe$_2$) is a transition metal dichalcogenide whose physical properties depend critically on the number of layers. In this paper, we use apertureless scattering-type near-field optical microscopy operating at Terahertz (THz) frequencies and cryogenic temperatures to identify distinct THz range electromagnetic behavior of WTe$_2$ mono-, bi- and tri-layer terraces in the same micro-crystals. We observed clear metallic behavior of the near-field signal on tri-layer regions. Our data are consistent with the existence of surface plasmon polaritons (SPP) in the THz range confined to tri-layer terraces in our specimens. The near-field signal on bi-layer regions surprisingly shows moderately metallicity, but with negligible temperature dependence. Subdiffractional THz imaging data together with theoretical calculations considering thermally activated carriers favor the semimetal scenario over the semiconductor scenario for bi-layer WTe$_2$. THz images for monolayer terraces uncovered weakly insulating behavior consistent with transport data.

The physical properties of the enigmatic material Tungsten ditelluride (WTe_2) is determined critically on the number of layers. Bulk WTe_2 is postulated to be a type-II Weyl semimetal [1] [2] with Fermi-arc surface states. Mono-layer WTe_2 has been predicted and experimentally confirmed to be a quantum spin hall insulator [3] [4] [5] [6] [7] [8] and exhibits gate-induced superconductivity [9] [10]. Bi-layer WTe_2 has broken inversion symmetry and exhibit ferroelectric properties [11], yet the intrinsic semi metallic v.s. semiconducting nature of bilayers still remains unresolved experimentally. Bi-layers exhibit a narrow gap (<10 meV) semiconducting behavior in transport measurements [3]. Angle resolved photoemission spectroscopy (ARPES), however, revealed that bi-layers could also be weakly semimetallic with a small negative gap [12]. A combination of inverted bands, strong spin-orbit coupling and low crystal symmetry makes few-layer WTe_2 an ideal system for studying topological effects such as the nonlinear anomalous Hall effect [13] [14] [15] and various unusual photogalvanic effects [16] [17] [18]. The goal of the present study is to explore the evolution of the low-energy electrodynamics of WTe_2 from monolayer to few-layer variants (Fig. 1a). We conclude that tri-layer specimens are metallic and host surface plasmon polaritons (SPP) [19] [20] that dominate the response in the terahertz (THz) range. Metallic response is reduced in bi-layer areas and completely disappeared in mono-layer regions.

Bulk WTe_2 exhibits high electronic mobility and its intraband (Drude) optical response is entirely contained in the THz region [21] [22]. Despite tremendous interests, THz response of monolayer and few-layer samples remains unexplored. THz experiments on few-layer WTe_2 specimens are challenging because of the minuscule size of available samples typically under 10x10 μm^2. The wavelength of THz waves is of the order of ~300 μm and conventional diffraction-limited methods are inadequate for interrogating the THz response of WTe_2 microcrystals. In order to overcome the diffraction limit in THz, we utilize a scattering-type THz scanning near-field optical microscope (THz-SNOM) [23] [24] [25] [26] [27]. This technique is a hybrid of an atomic force microscope (AFM) with a pulsed THz source. AFM-based THz nano-scopy offers a robust experimental approach to investigate materials with sub-diffractional spatial resolution down to $\lambda/2000$ where λ is the wavelength of the probe beam. THz-SNOMs are being successfully applied to an expanding list of materials and interesting problems. For example, THz-SNOM methods have provided insights into nano-scale studies of electronic phase separation in the vicinity of the insulator-to-metal transition in VO_2 [23], the plasmonic response of graphene [26] [28], free carrier distributions in nanodevices [29] [30], and phonon resonances in multiferroic materials [31]. Here we report on near-field nano-optical experiments in THz range for WTe_2 conducted at cryogenic temperature. The nano-THz measurements reveal that tri-layers of WTe_2 show metallic behavior and plasmonic response consistent with the properties of bulk crystal whereas bi-layer samples exhibit weak semimetallic behavior.

We investigated multi-terraced microcrystals of WTe$_2$ using a home-built apparatus enabling nano-THz experiments at cryogenic temperature [23]. The THz beam is focused onto an AFM tip with an 80 μm long shaft made of PtIr wire. The tip apex locally confines and enhances the THz electric field. The tip shaft functions as an antenna [32] and out-couples the near-field radiation into the far-field radiation reaching the photoconductive antenna (PCA) detector. The tapping of the tip modulates the near-field signal at ~70 kHz. We demodulated the amplitude of the tip-scattered electric field at the first (S_1) and the second (S_2) harmonics of the tip tapping frequency to suppress the undesired far-field background [23] [33].
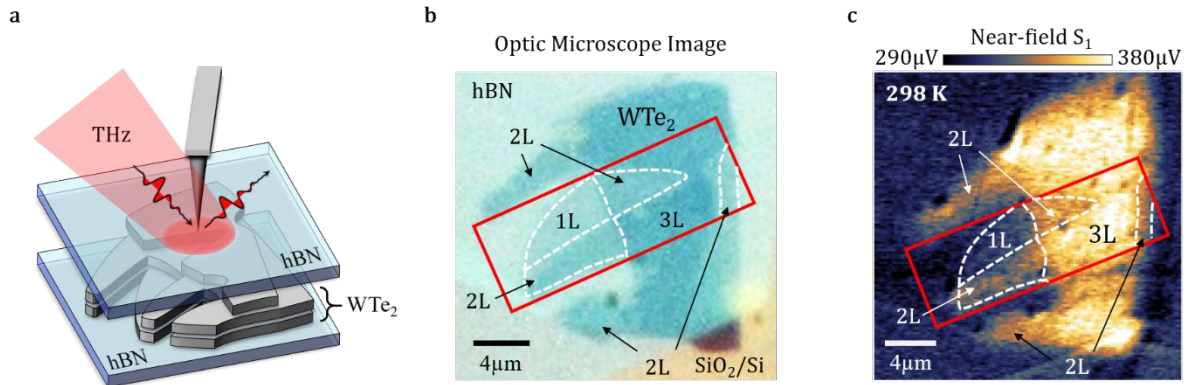
**Figure 1|Schematic of nano-THz experiments on multi-terraced crystals of WTe$_2$. a** Metallic AFM tip locally enhances the electric field and enables THz coupling to materials at length scales much smaller than the THz wavelength. The size of the focused THz beam in the schematic is much smaller than the real focus. **b** Optical microscope image of the WTe$_2$ sample. Multi-terraced microcrystals of WTe$_2$ are encapsulated on top and bottom with hexagonal boron nitride (hBN) and reside on the SiO$_2$/Si substrate. Optical inspection reveals mono-, bi-, and tri-layer regions. The red frame indicates the field of view used for temperature dependent study in Fig. 2. We mark the boundaries of terraces with different number of WTe$_2$ layers (1L, 2L, 3L) with dashed lines. **c** THz near-field signal S$_1$ at room temperature, showing much higher THz signal in the tri-layer region compared to mono- and bi-layers.

The exfoliated micro-crystals of WTe$_2$ is encapsulated between 6 nm of hexagonal boron nitride (hBN) on top and 20 nm hBN on the bottom (Fig.1a). The exfoliated structure is assembled on top of a SiO$_2$/Si wafer. This sample reveals terraces of mono-, bi-, and tri-layer WTe$_2$ within a 25×25 μm^2 area. These terraces are evident in both the optical inspection image (Fig.1b) and in the nano-THz scan displaying the contrast in the scattering amplitude of the THz signal (Fig. 1c). The topographic contrast of AFM scans has only limited utility in visualizing the terraces because this contrast is suppressed by the top encapsulating layer (Supplementary Note 1). We obtained the network of dashed lines in Fig. 1b and c using a combination of optical contrast and nano-THz contrast. We remark that the top layer hBN is thin enough that the evanescent field from the sample is still detectable with the help of the AFM antenna tailored for the THz range.

In nano-THz experiments, the near-field scattering amplitude is an observable carrying information on spatially localized electromagnetic response [33] [34] [35] [36]. The

measured signal is denoted by $S_{1,2} \propto |\tilde{E}^{NF}|$ where $\tilde{E}^{NF}$ is the THz near-field electric field. We analyzed the so-called approach curves: the variation of the $S_{1,2}$ signal as a function of separation between the tip and the sample (see Supplementary Note 2). This analysis confirmed that over 90% of the signal demodulated at the second harmonic of the tapping frequency S_2 originates from the near-field tip-sample interaction within 150nm above the sample surface [37]. Demodulation of the THz signal at higher harmonics is not practical in view of the rapidly diminishing signal-to-noise ratio already at the third harmonic. The far-field contribution is enhanced at higher optical frequencies outside of the THz range [33]. For that reason, nano-optical experiments conducted in the mid-IR and visible ranges typically require demodulation at the third, fourth or even fifth harmonics [33]. In our nano-THz experiments, the tip radius is $R = 150 - 200$ nm as determined by scanning electron microscopy. The tapping amplitude is ~150 nm. The tip radius and the tapping amplitude govern the center momentum (0.1/R~1/R) for photon scattering by the tip [38] [39] and the achievable spatial resolution [37].

Here we report nano-THz imaging data collected in frequency-integrated mode at every pixel. The frequency range of the THz radiation in our experiments spans between 0.2 THz and 2.5 THz. Due to the antenna resonance effect of the tip, the near-field signal intensity is peaked at ~0.6 THz [23] [40]. Our nano-THz apparatus is designed to produce hyperspectral images with fully spectrally resolved information at every pixel by Fourier transforming the time-domain spectra [41]. However, energy-integrated or "white-light" THz imaging has an important advantage of significantly increasing the signal-to-noise required to produce high fidelity images of weakly absorbing few-layer WTe_2 samples presented in Figs. 1, 2. We accompany nano-THz data with images in the infrared range where we employ a monochromatic light source (Supplementary Note 5).
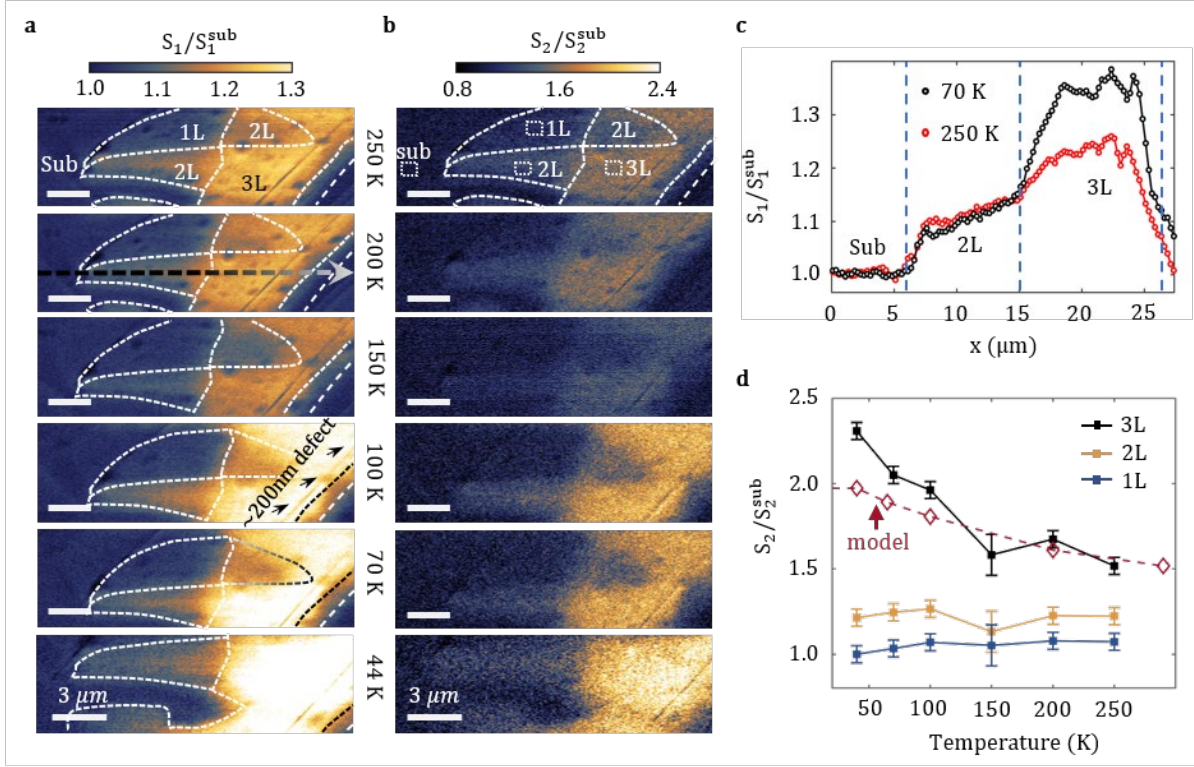
Figure 2|Temperature dependent near-field maps of nano-THz response of WTe₂ micro-crystals. The scale bars in all panels are 3 μm. **a** Near-field images of the normalized amplitude contrast S_1/S_1^{sub} of nearly identical regions at 6 different temperatures between 250 K and 44 K. Broadband THz signal utilized in these images shows intensity peaked at 0.6 THz. S_1^{sub}: the signal due to the SiO₂/Si substrate has negligible temperature dependence in the THz range studied here. The horizontal dashed arrow in the panel at 200 K indicates the scanning line-cut used to construct the plot in Fig.2c. Micrometer-sized dark spots also visible in the topographic AFM contrast can be attributed to bubbles in the encapsulated structures. **b** Near-field S_2/S_2^{sub} images taken simultaneously with S_1/S_1^{sub}. **c** S_1/S_1^{sub} line-cut (averaged over 5 neighboring pixels) at 250 K and 70 K. The line-cut corresponds to the arrow in Fig.2a. **d** Normalized S₂ signals averaged in the regions indicated in the S₂ images (white dashed boxes) for the substrate and for monolayer, bilayer, tri-layer regions of WTe₂. The filled squares are experimental data and the dashed line is model calculation discussed in the text.

In Figure 2, we show the complete set of temperature dependent THz nano-imaging data. We plot the scattering amplitude signals S_1 and S_2 normalized by those of the SiO₂/Si substrate S^{sub}: S_1/S_1^{sub} and S_2/S_2^{sub}. The S_1 data have roughly 2 times higher signal to noise ratio (SNR) than S_2. Both S_1 and S_2 images display the same gross features. Since S_2 is more sensitive to the intrinsic local electrodynamics, we rely on S_2 to quantify the temperature dependence of the near-field response in the analysis that follows. We confirmed that the near-field signal due to the SiO₂/Si substrate shows negligible temperature dependence. We therefore used the signal produced by the bare substrate as a reference in our normalization procedure. In all THz images, we clearly resolve a feature due to a ~200nm wide topographic linear defect marked in the panel obtained at T=100K. This latter topographic feature confirms that the spatial resolution of our THz near-field imaging is well below ~200nm at all temperatures.

In order to analyze the contrast between terraces with different number of WTe$_2$ layers, horizontal line-cuts from the S_1 images are displayed in Fig. 2d. The location of the line-cut is indicated with a dashed arrow in the 200 K image of Fig. 2a. The line-cut shows evident plateaus corresponding to terraces with different number of layers. Regions with a higher number of layers exhibit higher near-field signal. The signal on the tri-layer region increased substantially at lower temperature, consistent with usual metallic response. Mono-layers (Supplementary Note 3) are marginally distinguishable from the substrate, demonstrating a clear insulating response. The bi-layer region, however, showed an interesting combination of its mono- and tri-layer counterparts. While the overall near-field signal is 10%~15% higher than the insulating mono-layer, the absence of any temperature dependence strongly restricts the size and the sign of its mysterious bandgap, as we will discuss below. Near-field data is extracted in small areas in the center of three different terraces to analyze S_2 signal trends. These areas are indicated as white dashed rectangles in the image taken at 250K in Fig. 2b. The temperature dependence of nano-THz contrast extracted from this analysis is plotted in Fig. 2e. The signal in the tri-layer area increases by more than 40% between ambient and T=40K. whereas in bi-layer and mono-layer regions, the increase of signal at low temperature is absent.

It is instructive to compare the temperature dependence of the THz near-field contrast summarized in Fig. 2e with DC transport data [3]. The DC conductivity of tri-layer WTe$_2$ is metallic at all temperatures in agreement with the nano-THz trend we report in Fig. 2e. For bi-layer WTe$_2$, DC transport data indicate a semiconducting behavior with a narrow gap in the meV range [3]. Specifically, the DC conductivity drops significantly below 100 K [3]. In many conducting materials, the real part of the optical conductivity in the THz range matches the DC value. However, if a material has a THz-range gap, this will not be the case. Indeed, the temperature independent nano-THz response of the bi-layer terraces contrasts with the drop of the DC conductivity in undoped bilayer WTe$_2$ at low temperature. We note that hBN encapsulated WTe$_2$ is normally found to be almost undoped and therefore extrinsic doping of this sample is unlikely [3].

Nano-THz imaging data presented in the form of two-dimensional maps in Fig. 2a, b or line-cuts in Fig. 2c reveal a significant spatial dependence of the scattering signal. This effect is vividly manifested as a gradual change in both the S_1 and S_2 signal within a 2-3 μm vicinity of the boundaries of tri-layer WTe$_2$. We remark that the width of these transitional regions is significantly larger than the spatial resolution of our near-field imaging apparatus (~200nm), as well as the width of the physical boundary observed in Fig. 1. Comparing the line-cut curves acquired at different temperatures in Fig. 2d, the location and the width of the transitional region with a gradual changing signal has no noticeable dependence on temperature. With the help of real-space near-field modeling of SPP on confined structure presented in the latter part of the paper, we show that the gradual spatial variation of the signal potentially arises from THz SPPs with long wavelength (8~16 μm).

We now discuss our data in the context of recent observation of edge states in WTe$_2$ [4] [6]. In Supplementary Fig. 3, we further zoom in onto the monolayer region at the lowest

temperature, 44 K. If edge states produced contrast in the THz range, we would see signal near the boundary between the monolayer WTe$_2$ and hBN/SiO$_2$/Si substrate and possibly additional boundaries between monolayer and bi-layer WTe$_2$. Indeed, such signals near the boundary are seen in the GHz regime [4]. However, we observe no significant signal at the boundaries of the monolayer. This implies that the electrodynamic response of the edge state does not extend to the 0.5-1.5 THz range within our SNR resolution (30:1 in S1).
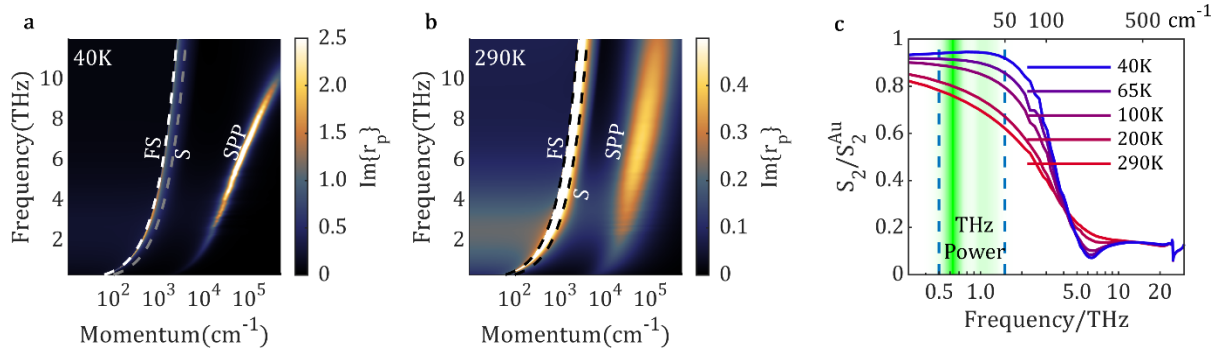
Figure 3|Electrodynamics and plasmonic response of tri-layer WTe$_2$. Imaginary part of the momentum dependent p-polarized reflection coefficient $r_p(\omega, q)$ at **a** 40 K and **b** 290 K, based on bulk dielectric function data *[21]*. Free space (FS) and SiO$_2$ (S) light lines are indicated with white and grey dashed lines, respectively. SPP dispersions are clearly observed and the dispersion broadens with increasing temperature. **c** Spectra of the near-field scattering amplitude modeled following Ref. *[42]* at different temperatures based on calculated $r_p(\omega, q)$. The shaded area indicates the frequency spectrum of our THz source.

To understand the THz near-field contrast of WTe$_2$ microcrystals, we carried out modeling of the response associated with the tri-layer region. We assume that the optical constants of the tri-layers can be accurately represented by far-field data for bulk WTe$_2$ [21]. In our analysis we take into account encapsulating hBN layers as well as the response of the SiO$_2$/Si substrate within the framework of a multilayer model of the near-field response described in Ref. [42]. An implicit assumption of the model in Ref. [42] is that all layers in multi-layered structures are either isotropic or uniaxial with an out-of-plane optical axis. On the contrary, WTe$_2$ reveals notable in-plane anisotropy with distinct plasma frequencies between a and b axes within the WTe$_2$ plane [21] [22]. In the analysis that follows, we assumed that tri-layer WTe$_2$ can be reasonably described as a uniaxial material with its in-plane relative permittivity represented by that of b-axis of bulk WTe$_2$. We also performed calculations with both a purely a-axis response and an effective dielectric function averaging between a-axis and b-axis data. All three methods produce qualitatively similar results (Supplementary Note 4).

We proceed with the quantitative analysis of the nano-THz response of WTe$_2$ tri-layers by calculating the p-polarized reflectivity $r_p(\omega, q)$ following the procedure described in ref [42]. The imaginary part of $r_p(\omega, q)$ (Fig. 3a) reveals strongly dispersing SPP. The three modes in Figs. 3a and 3b are, from left to right, the free-space light line, the light line in SiO$_2$ and the SPP in tri-layer WTe$_2$. The SPP is very sharp at low temperatures, while at 290 K it is overdamped. This is due to reduced scattering of electrons at low temperature [43] [44].

The dispersion calculation in Fig. 3a and 3b implies that the SPP wavelength is as long as 8~16 μm in the THz range. Because the tips we utilize in nano-THz experiments have radii R=150~200 nm, we gain access to the range of momenta peaked around $0.1/R \sim 5 \times 10^3$ cm^{-1} [38] [39] [42]. Since the THz intensity in our experiments is spread over 0.5-1.5 THz, we can extract the accessible range of wavelengths of the SPP modes from Fig. 3a. This straightforward procedure suggests that the relevant modes occur between 4×10^3 cm^{-1} and 8×10^3 cm^{-1}, implying that the wavelengths of these modes span the range between 8~16 μm. THz near-field tip is thus expected to efficiently couple to SPP modes in tri-layer WTe$_2$.

Next, we calculated the near-field spectra of WTe$_2$ based on $r_p(\omega, q)$ dispersion calculations. In Fig. 3b, we show the near-field amplitude spectrum produced within the framework of a lightning-rod model [42] at different temperatures. In the 0.5 - 1.5 THz range, the measured near-field signal is governed by the SPP of WTe$_2$. At low temperatures, plasmonic losses due to electron-phonon scattering are reduced and the SPP mode becomes more pronounced. The model results can be directly compared with experimental data. By integrating the near-field signal at all frequencies investigated with our THz apparatus (shaded region in Fig. 3c), we acquired the model near-field signal at all temperatures. The result is plotted in Fig. 2d (red dashed line) along with the experimental data. This analysis captured the gross features of the temperature dependence of the experimental data. We therefore conclude that the additional increase of signal at low temperature is linked to the SPP response in tri-layer WTe$_2$.

While the presence of a large gap of >60 meV in monolayer WTe$_2$ is demonstrated by transport [3] and ARPES [12] measurements, the semiconductor versus semimetallic nature of the bilayer remains unclear. ARPES experiments on bi-layer WTe$_2$ [12] indicate a vanishing, if not negative, gap(Fig. 4d and 4e). Transport measurements indicate semiconducting/insulating behavior with a small gap (<10 meV) [3] (Fig. 4e). Our local nano-THz experiments provide a unique probe in the relevant frequency region, without complications from electrical contacts and inevitable defects. The pronounced temperature dependence observed in metallic tri-layers is rooted in the increase of Drude scattering rate (γ) with temperature (T), following $\gamma \propto T^2$ for a Fermi liquid [43]. The complete insulating behavior of mono-layer areas is likely due to its large gap (>60 meV). On bi-layer WTe$_2$, the fact that its near-field signal is higher than mono-layer WTe$_2$ requires a weak metallicity (Supplementary Note 5).

Within the small gap or negative gap scenario, thermally activated carriers are the main contributor to the weak metallicity of bi-layer WTe$_2$. In Fig. 4, we theoretically investigated the temperature dependence of near-field signal due to the thermally activated carriers in bi-layer WTe$_2$ with different gap sizes (Supplementary Note 5). In Fig. 4a, when the gap size is in the range of -10 meV to 10 meV, the carrier density at 40 K is as high as n_{2D}=0.2~1e12 cm^{-2}, which is smaller than the value (3.6e12 cm^{-2}) reported in ARPES experiment [12]. The temperature dependence of the scattering rate and of the carrier density dictate the temperature dependence of the near-field response. As is shown in Fig.

4b, thermally activated carriers directly contribute to the signal measured in our experiment.
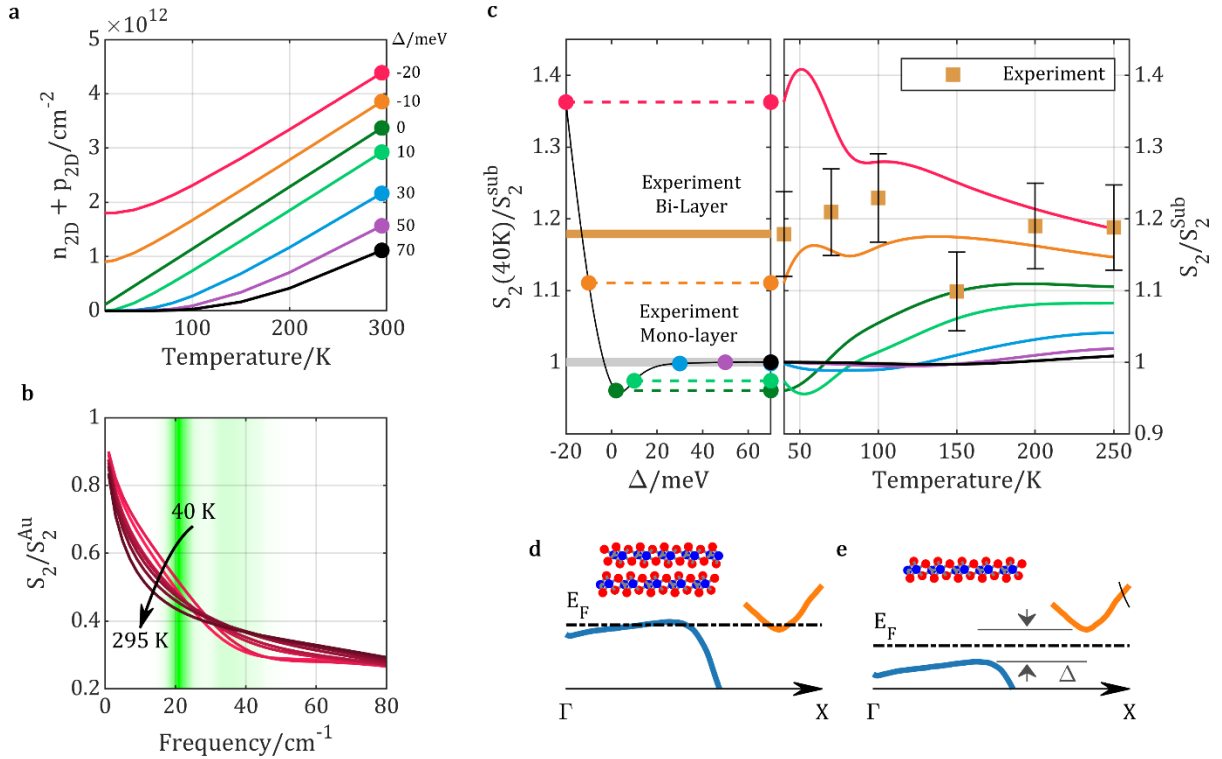
Figure 4|Near-field electrodynamics of thermally activated carrier of WTe₂. a Temperature dependence of thermally activated carrier densities at different gap sizes calculated (Supplementary Note 5) based on the band structure investigated by ARPES *[12]*. **b** Near-field spectroscopic response of the thermally activated carriers of a model bi-layer WTe2 with $\Delta = -10~meV$. The green shaded region represents the power spectrum of the THz probe. **c** Right panel: Temperature dependent white-light near-field signals for bi-layer WTe₂ with gap sizes ranging from -20 meV to 70 meV. Along with the model, nano-THz data of bi-layer WTe₂ are displayed with yellow square. Both the model curves and experiment points are normalized to the substrate value. Left panel: The gap-size dependent near-field signal of bi-layer at 40 K. The signal level is strongly suppressed when the gap is close to zero or positive. **d, e** Hypothetical band structure of semimetallic bi-layer WTe₂ (left) and insulating mono-layer WTe₂ *[12]* with a bandgap Δ>60 meV (right).

The temperature dependence of the white-light near-field signal corresponding to different gap sizes of bi-layer WTe₂ are displayed in Fig. 4c (right panel). When the gap size is larger than 10 meV, thermally activated carrier density is sufficiently low that the near-field response in THz range resembles an insulator. This "large gap" scenario (compared to our THz probe) explains the low signal level for mono-layer regions in Fig. 2. When the gap size is reduced below +10 meV, the near-field signal at high temperature gradually increases and is comparable to the experiment value. However, the carrier density (Fig. 4a) at low temperature gradually vanishes, leading to a strong suppression of the near-field signal at low temperatures. The temperature independent behavior for bi-layer WTe₂ observed in the experiment (square dots in Fig. 4c) therefore calls for a finite carrier density even at the lowest temperature (40 K), which favors the semimetallic scenario. Once the gap size is reduced to -10 meV (overlapping conduction and valence band), the signal at low

temperature becomes comparable to that at high temperature and better fits the experiment value (Fig. 4c). Further increasing the absolute negative gap (-20 meV) leads to an increase of near-field signal at low temperatures to the levels exceeding data for bi-layer WTe2, due to the abundance of carriers (Fig. 4a). The gap-size dependent near-field signal at T=40 K is summarized in Fig. 4c (left panel). Therefore, our observation of the temperature independent white-light signal on bi-layer WTe2 favors the semimetallic nature with a small negative gap ($\Delta\sim$-10 meV).
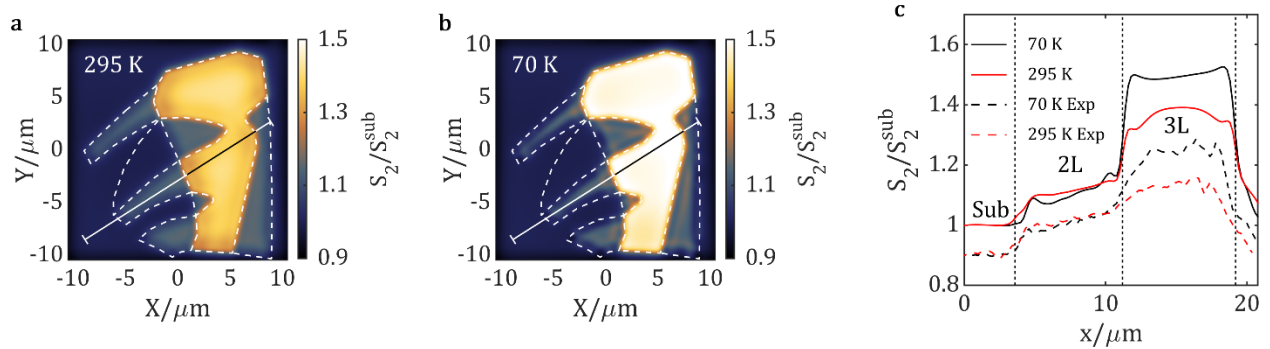

Figure 5| **a, b** Modeling of real-space near-field (S_1/S_1^{sub}) pattern associated with SPP at 295 K (**a**) and 70 K (**b**) on the investigated sample geometry. Dashed lines highlight the physical boundaries of all regions. Line-cuts across bi- and tri-layer WTe2 are indicated by the solid line in both images. **c** Model S_1/S_1^{sub} line-cuts extracted from **a** and **b** are plotted in solid lines. Along with the model result, experiment line-cuts are displayed in dashed lines and are shifted vertically for clarity.

With the knowledge of THz electrodynamic properties of mono-, bi- and tri-layer regions on our WTe2 microcrystal, it is now possible to model the real-space pattern of the THz near-field on the entire investigated sample as shown in Fig. 5. Following the analysis in Fig. 3 and Fig. 4, we assigned optical constants of bulk WTe2 for tri-layer regions. We used semimetal model with -10 meV gap for bi-layer regions and we adopted permittivity extracted from DFT calculation [45] for the mono-layer region. The real-space modeling in Fig. 5 considers the intrinsic SPP mode on the experimentally measured geometrical configuration of the microcrystals. Further details of this real-space calculation are provided in the Supplementary Note 6.

The real-space near-field modeling results for few-layer WTe2 (Fig. 5a and 5b) are in excellent agreement with the experiment images (Fig. 1c, Fig. 2a and 2b). In Fig. 5c, line-cuts were extracted at the same location with Fig. 2 and are compared with the experiment results. In case of bi-layer, the model perfectly reproduced the signal level and the slope of the signal from the substrate side to the tri-layer side. The model indicates higher signal for tri-layer regions compared with the experimental result. This difference can be explained by the potential deviation of tri-layer optical properties from the bulk (larger scattering rate or lower plasma frequency). Importantly, the gradual transition of near-field signal on bi- and tri-layer edges are present in both experiment and model results, proving that the blurred edges are caused by the long wavelength of the THz range SPPs. Because the wavelength of SPPs in tri-layer WTe2 is 8~16 µm, larger samples are required to image the complete fringe pattern of THz range SPPs of tri-layer WTe2. As for bi-layer WTe2, despite

the low carrier density, the near-field response of SPPs can be detected in THz frequencies and is strongly impacted by the thermally activated carriers. According to Fig. 4c, similar response is also expected in weak semiconductors at high temperature.

In conclusion, we investigated the low temperature nanoscale electromagnetic response of few-layer WTe$_2$ micro-crystals at THz frequencies. The low-temperature near-field signal has a strong dependence on the number of layers. The response of tri-layer WTe$_2$ is clearly metallic as evidenced by the temperature dependence and is dominated by SPPs in the confined geometry of narrow terraces. The extremely weak response of mono-layers are consistent with an insulator with relatively large bandgap. Surprisingly, bi-layer WTe$_2$ shows higher THz signal than insulating monolayers but the observed THz response is also independent of temperature from 250 K to 40 K. This latter behavior implies finite carrier density in bi-layers down to the lowest temperature of this experiment (40 K). Further modeling favors a semimetallic scenario with a small negative gap $|\Delta| < 10$ meV for bi-layer WTe$_2$. Finally, the complete knowledge of the electrodynamics of mono-, bi- and tri-layer WTe$_2$ in our sample allows for a direct real-space modeling of the THz near-field signal, which matches perfectly with the experiment. Our complete temperature dependent THz near-field images together with theoretical modeling paves the way for understanding the low energy electrodynamics of future quantum materials beyond the diffraction limit.

Methods:

THz scanning-type near-field optical microscope (THz-SNOM) [23]. Both the AFM scanner and focusing optics of our apparatus (Fig.1a) are situated in an ultra-high vacuum (UHV) compartment. This allows for measurements at temperatures down to ~40Klimited by the imperfect thermal contact of a sample carrier introduced through rapid access load locks into our UHV system. We utilize a pair of low temperature-grown GaAs photoconductive antennas (PCA, Neaspec GmbH) as emitter and detector. We activate both PCAs with a 1550nm femtosecond fiber laser after doubling its frequency in a nonlinear crystal.

In this experiment, we exploit the frequency-integrated (white-light) signal to produce high fidelity images. When a THz pulse is scattered by the tip and reaches to the detector, we can measure this pulse at different time point t_m. If we tune t_m to the main peak of the detected pulse where the phases of all frequency components in the wave packet are roughly equal, the white-light signal is acquired. For tri-layer WTe$_2$, the near-field spectra are almost flat (Fig. 3c). Therefore, white-light images are suitable to track its temperature dependence. For bi-layer and mono-layer regions, because of the low signal level, white-light images are needed to produce meaningful results.

Preparation of WTe$_2$ microcrystal.

WTe$_2$ crystals are mechanically exfoliated onto highly p-doped silicon substrates consisting of 285 nm SiO$_2$ [46]. WTe$_2$ flakes of mono- to tri-layers are optically identified and encapsulated within hBN flakes using standard polymer-based dry transfer technique. The top and bottom hBN flakes used for encapsulation are typically 5-7 nm thick and 12-30 nm thick, respectively. Both WTe$_2$ exfoliation and encapsulation processes are performed inside a nitrogen glovebox (oxygen and water vapor levels are less than 0.5 ppm). The polymer on top of the heterostructures are dissolved outside the glovebox before near-field optical measurements.

Lightning-rod model calculations of near-field signals. We mainly follow the modeling procedure described in Ref. [42]. The modeling is based on reflection coefficient $r_p(\omega, q)$ of the layered structure of the sample. A numerical solution to the electric field distribution of a tip-sample system is used to calculate near-field signal. In this way, parameters like tip radius and tapping amplitude is considered in the modeling. However, because the model is based on a 19μm long metallic tip with a cone structure. It does not account for the resonance of the 80μm tip to THz beam in the experiment. Our solution is to manually multiply the model spectra with the spectra measured on Au and use it as an approximation to experiment result.

Author contributions:

D.N.B., R.J. and Y.S. conceived the experiments. R.J. and Y.S. performed the THz-near-field imaging experiments. Z.F., D.H.C. and X.X. fabricated the WTe$_2$ devices. R.J., F.L.R, J.S., A.S.M. and M.M.F. conducted the lightning-rod modeling. C.F.B.L and A.S.M. performed real-space near-field modeling, Z.S, X.C. and M.L. provided helpful comments on the interpretation of the data. R.J., Y.M.S. and D.N.B. wrote the paper with input from all coauthors. D.N.B. supervised the project.

References

[1] P. Li, Y. Wen, X. He, Q. Zhang, C. Xia, Z.-M. Yu, S. A. Yang, Z. Zhu, H. N. Alshareef and X.-X. Zhang, "Evidence for topological type-II Weyl semimetal WTe 2," *Nature communications,* vol. 8, p. 2150, 2017.

[2] A. A. Soluyanov, D. Gresch, Z. Wang, Q. Wu, M. Troyer, X. Dai and B. A. Bernevig, "Type-ii weyl semimetals," *Nature,* vol. 527, p. 495–498, 2015.

[3] Z. Fei, T. Palomaki, S. Wu, W. Zhao, X. Cai, B. Sun, P. Nguyen, J. Finney, X. Xu and D. H. Cobden, "Edge conduction in monolayer WTe 2," *Nature Physics,* vol. 13, p. 677, 2017.

[4] Y. Shi, J. Kahn, B. Niu, Z. Fei, B. Sun, X. Cai, B. A. Francisco, D. Wu, Z.-X. Shen, X. Xu and others, "Imaging quantum spin Hall edges in monolayer WTe2," *Science advances,* vol. 5, p. eaat8799, 2019.

[5] L. Peng, Y. Yuan, G. Li, X. Yang, J.-J. Xian, C.-J. Yi, Y.-G. Shi and Y.-S. Fu, "Observation of topological states residing at step edges of WTe 2," *Nature communications,* vol. 8, p. 659, 2017.

[6] S. Tang, C. Zhang, D. Wong, Z. Pedramrazi, H.-Z. Tsai, C. Jia, B. Moritz, M. Claassen, H. Ryu, S. Kahn and others, "Quantum spin Hall state in monolayer 1T'-WTe 2," *Nature Physics,* vol. 13, p. 683, 2017.

[7] S. Wu, V. Fatemi, Q. D. Gibson, K. Watanabe, T. Taniguchi, R. J. Cava and P. Jarillo-Herrero, "Observation of the quantum spin Hall effect up to 100 kelvin in a monolayer crystal," *Science,* vol. 359, p. 76–79, 2018.

[8] X. Qian, J. Liu, L. Fu and J. Li, "Quantum spin Hall effect in two-dimensional transition metal dichalcogenides," *Science,* vol. 346, p. 1344–1347, 2014.

[9] E. Sajadi, T. Palomaki, Z. Fei, W. Zhao, P. Bement, C. Olsen, S. Luescher, X. Xu, J. A. Folk and D. H. Cobden, "Gate-induced superconductivity in a monolayer topological insulator," *Science,* vol. 362, p. 922–925, 2018.

[10] V. Fatemi, S. Wu, Y. Cao, L. Bretheau, Q. D. Gibson, K. Watanabe, T. Taniguchi, R. J. Cava and P. Jarillo-Herrero, "Electrically tunable low-density superconductivity in a monolayer topological insulator," *Science,* vol. 362, p. 926–929, 2018.

[11] Z. Fei, W. Zhao, T. A. Palomaki, B. Sun, M. K. Miller, Z. Zhao, J. Yan, X. Xu and D. H. Cobden, "Ferroelectric switching of a two-dimensional metal," *Nature,* vol. 560, p. 336, 2018.

[12] I. Cucchi, I. Gutiérrez-Lezama, E. Cappelli, S. McKeown Walker, F. Y. Bruno, G. Tenasini, L. Wang, N. Ubrig, C. Barreteau, E. Giannini and others, "Microfocus laser–angle-resolved photoemission on encapsulated mono-, bi-, and few-layer 1T'-WTe2," *Nano letters,* vol. 19, p. 554–560, 2018.

[13] I. Sodemann and L. Fu, "Quantum nonlinear Hall effect induced by Berry curvature dipole in time-reversal invariant materials," *Physical review letters,* vol. 115, p. 216806, 2015.

[14] K. Kang, T. Li, E. Sohn, J. Shan and K. F. Mak, "Nonlinear anomalous Hall effect in few-layer WTe 2," *Nature materials,* vol. 18, p. 324, 2019.

[15] Q. Ma, S.-Y. Xu, H. Shen, D. MacNeill, V. Fatemi, T.-R. Chang, A. M. M. Valdivia, S. Wu, Z. Du, C.-H. Hsu and others, "Observation of the nonlinear Hall effect under time-reversal-symmetric conditions," *Nature,* vol. 565, p. 337, 2019.

[16] S.-Y. Xu, Q. Ma, H. Shen, V. Fatemi, S. Wu, T.-R. Chang, G. Chang, A. M. M. Valdivia, C.-K. Chan, Q. D. Gibson and others, "Electrically switchable Berry curvature dipole in the monolayer topological insulator WTe 2," *Nature Physics,* vol. 14, p. 900–906, 2018.

[17] Q. Wang, J. Zheng, Y. He, J. Cao, X. Liu, M. Wang, J. Ma, J. Lai, H. Lu, S. Jia and others, "Robust edge photocurrent response on layered type II Weyl semimetal WTe 2," *Nature Communications,* vol. 10, p. 1–7, 2019.

[18] Z. Ji, W. Liu, S. Krylyuk, X. Fan, Z. Zhang, A. Pan, L. Feng, A. Davydov and R. Agarwal, "Photocurrent detection of the orbital angular momentum of light," *Science,* vol. 368, p. 763–767, 2020.

[19] D. N. Basov, M. M. Fogler and F. G. De Abajo, "Polaritons in van der Waals materials," *Science,* vol. 354, p. aag1992, 2016.

[20] T. Low, A. Chaves, J. D. Caldwell, A. Kumar, N. X. Fang, P. Avouris, T. F. Heinz, F. Guinea, L. Martin-Moreno and F. Koppens, "Polaritons in layered two-dimensional materials," *Nature materials,* vol. 16, p. 182–194, 2017.

[21] A. J. Frenzel, C. C. Homes, Q. D. Gibson, Y. M. Shao, K. W. Post, A. Charnukha, R. J. Cava and D. N. Basov, "Anisotropic electrodynamics of type-II Weyl semimetal candidate WTe 2," *Physical Review B,* vol. 95, p. 245140, 2017.

[22] C. Wang, S. Huang, Q. Xing, Y. Xie, C. Song, F. Wang and H. Yan, "Van der Waals thin films of WTe 2 for natural hyperbolic plasmonic surfaces," *Nature communications,* vol. 11, p. 1–9, 2020.

[23] H. T. Stinson, A. Sternbach, O. Najera, R. Jing, A. S. Mcleod, T. V. Slusar, A. Mueller, L. Anderegg, H. T. Kim, M. Rozenberg and others, "Imaging the nanoscale phase separation in vanadium dioxide thin films at terahertz frequencies," *Nature communications,* vol. 9, p. 3604, 2018.

[24] H.-G. Von Ribbeck, M. Brehm, D. W. Van der Weide, S. Winnerl, O. Drachenko, M. Helm and F. Keilmann, "Spectroscopic THz near-field microscope," *Optics Express,* vol. 16, p. 3430–3438, 2008.

[25] K. Moon, Y. Do, M. Lim, G. Lee, H. Kang, K.-S. Park and H. Han, "Quantitative coherent scattering spectra in apertureless terahertz pulse near-field microscopes," *Applied Physics Letters,* vol. 101, p. 011109, 2012.

[26] J. Zhang, X. Chen, S. Mills, T. Ciavatti, Z. Yao, R. Mescall, H. Hu, V. Semenenko, Z. Fei, H. Li and others, "Terahertz nanoimaging of graphene," *ACS Photonics,* vol. 5, p. 2645–2651, 2018.

[27] N. A. Aghamiri, F. Huth, A. J. Huber, A. Fali, R. Hillenbrand and Y. Abate, "Hyperspectral time-domain terahertz nano-imaging," *Optics express,* vol. 27, p. 24231–24242, 2019.

[28] F. H. L. Koppens, T. Mueller, P. Avouris, A. C. Ferrari, M. S. Vitiello and M. Polini, "Photodetectors based on graphene, other two-dimensional materials and hybrid systems," *Nature nanotechnology,* vol. 9, p. 780, 2014.

[29] A. J. Huber, F. Keilmann, J. Wittborn, J. Aizpurua and R. Hillenbrand, "Terahertz near-field nanoscopy of mobile carriers in single semiconductor nanodevices," *Nano letters,* vol. 8, p. 3766–3770, 2008.

[30] Z. Yao, V. Semenenko, J. Zhang, S. Mills, X. Zhao, X. Chen, H. Hu, R. Mescall, T. Ciavatti, S. March and others, "Photo-induced terahertz near-field dynamics of graphene/InAs heterostructures," *Optics express,* vol. 27, p. 13611–13623, 2019.

[31] L. Wehmeier, T. Nörenberg, T. V. A. G. de Oliveira, J. M. Klopf, S.-Y. Yang, L. W. Martin, R. Ramesh, L. M. Eng and S. C. Kehr, "Phonon-induced near-field resonances in multiferroic BiFeO3 thin films at infrared and THz wavelengths," *Applied Physics Letters,* vol. 116, p. 071103, 2020.

[32] F. Huth, A. Chuvilin, M. Schnell, I. Amenabar, R. Krutokhvostov, S. Lopatin and R. Hillenbrand, "Resonant antenna probes for tip-enhanced infrared near-field microscopy," *Nano letters,* vol. 13, p. 1065–1072, 2013.

[33] A. J. Sternbach, J. Hinton, T. Slusar, A. S. McLeod, M. K. Liu, A. Frenzel, M. Wagner, R. Iraheta, F. Keilmann, A. Leitenstorfer and others, "Artifact free time resolved near-field spectroscopy," *Optics Express,* vol. 25, p. 28589–28611, 2017.

[34] M. Böhmler, A. Huber and M. Eisele, "THz nano-spectroscopy with 25 nm spatial and 10 fs time resolution," in *2016 41st International Conference on Infrared, Millimeter, and Terahertz waves (IRMMW-THz)*, 2016.

[35] K. Moon, H. Park, J. Kim, Y. Do, S. Lee, G. Lee, H. Kang and H. Han, "Subsurface nanoimaging by broadband terahertz pulse near-field microscopy," *Nano letters,* vol. 15, p. 549–552, 2014.

[36] S. T. Chui, X. Chen, M. Liu, Z. Lin and J. Zi, "Scattering of electromagnetic waves from a cone with conformal mapping: Application to scanning near-field optical microscope," *Physical Review B,* vol. 97, p. 081406, 2018.

[37] C. Maissen, S. Chen, E. Nikulina, A. Govyadinov and R. Hillenbrand, "Probes for Ultrasensitive THz Nanoscopy," *ACS Photonics,* vol. 6, p. 1279–1288, 2019.

[38] B.-Y. Jiang, L. M. Zhang, A. H. Castro Neto, D. N. Basov and M. M. Fogler, "Generalized spectral method for near-field optical microscopy," *Journal of Applied Physics,* vol. 119, p. 054305, 2016.

[39] Z. Fei, G. O. Andreev, W. Bao, L. M. Zhang, A. S. McLeod, C. Wang, M. K. Stewart, Z. Zhao, G. Dominguez, M. Thiemens and others, "Infrared nanoscopy of Dirac plasmons at the graphene–SiO2 interface," *Nano letters,* vol. 11, p. 4701–4705, 2011.

[40] S. Mastel, M. B. Lundeberg, P. Alonso-González, Y. Gao, K. Watanabe, T. Taniguchi, J. Hone, F. H. L. Koppens, A. Y. Nikitin and R. Hillenbrand, "Terahertz nanofocusing with cantilevered terahertz-resonant antenna tips," *Nano letters,* vol. 17, p. 6526–6533, 2017.

[41] D. Grischkowsky, S. Keiding, M. Van Exter and C. Fattinger, "Far-infrared time-domain spectroscopy with terahertz beams of dielectrics and semiconductors," *JOSA B,* vol. 7, p. 2006–2015, 1990.

[42] A. S. McLeod, P. Kelly, M. D. Goldflam, Z. Gainsforth, A. J. Westphal, G. Dominguez, M. H. Thiemens, M. M. Fogler and D. N. Basov, "Model for quantitative tip-enhanced spectroscopy and the extraction of nanoscale-resolved optical constants," *Physical Review B,* vol. 90, p. 085136, 2014.

[43] C. C. Homes, M. N. Ali and R. J. Cava, "Optical properties of the perfectly compensated semimetal WTe 2," *Physical Review B,* vol. 92, p. 161109, 2015.

[44] Y. Yi, C. Wu, H. Wang, H. Liu, H. Li, H. Zhang, H. He and J. Wang, "Thickness dependent magneto transport properties of WTe2 thin films," *Solid State Communications,* vol. 260, p. 45–49, 2017.

[45] H. Wang and T. Low, "Hyperbolicity in 2D transition metal ditellurides induced by electronic bands nesting," *arXiv preprint arXiv:2005.05416,* 2020.

[46] W. Zhao, Z. Fei, T. Song, H. K. Choi, T. Palomaki, B. Sun, P. Malinowski, M. A. McGuire, J.-H. Chu, X. Xu and others, "Magnetic proximity and nonreciprocal current switching in a monolayer WTe 2 helical edge," *Nature Materials,* vol. 19, p. 503–507, 2020.

[47] M. K. Liu, M. Wagner, E. Abreu, S. Kittiwatanakul, A. McLeod, Z. Fei, M. Goldflam, S. Dai, M. M. Fogler, J. Lu and others, "Anisotropic electronic state via spontaneous phase separation in strained vanadium dioxide films," *Physical review letters,* vol. 111, p. 096602, 2013.

[48] A. C. Jones, S. Berweger, J. Wei, D. Cobden and M. B. Raschke, "Nano-optical investigations of the metal- insulator phase behavior of individual VO2 microcrystals," *Nano letters,* vol. 10, p. 1574–1581, 2010.

[49] L. Wang, I. Gutiérrez-Lezama, C. Barreteau, N. Ubrig, E. Giannini and A. F. Morpurgo, "Tuning magnetotransport in a compensated semimetal at the atomic scale," *Nature communications,* vol. 6, p. 1–7, 2015.